inorganics

MDPI

Article

The Effect of Central Metal Ions (Dy, Er, Ni, and V) on the Structural and HSA-Binding Properties of 2-Hydroxy-3-methoxybenzaldehyde Semicarbazone Complexes

Violeta Jevtovic [1], Jelena M. Živković [2], Aleksandra A. Rakić [3], Aljazi Abdullah Alrashidi [1], Maha Awjan Alreshidi [1], Elham A. Alzahrani [1], Odeh A. O. Alshammari [1], Mostafa Aly Hussien [4] and Dušan Dimić [3,*]

[1] Department of Chemistry, College of Science, University of Ha'il, Ha'il 81451, Saudi Arabia; v.jevtovic@uoh.edu.sa (V.J.)
[2] Innovative Centre of the Faculty of Chemistry, Studentski trg 12-16, 11158 Belgrade, Serbia
[3] Faculty of Physical Chemistry, University of Belgrade, Studentski trg 12-16, 11158 Belgrade, Serbia
[4] Department of Chemistry, Faculty of Science, King Abdul Aziz University, Jeddah 21589, Saudi Arabia
* Correspondence: ddimic@ffh.bg.ac.rs

Abstract: 2-Hydroxy-3-methoxybenzaldehyde semicarbazone (HMBS) is a multidentate ligand with interesting coordination behavior that depends on the central metal ion and the overall complex geometry. In this contribution, the structural characteristics of five HMBS-containing complexes with different metal ions (Dy, Er, Ni, and V) were investigated. Four binuclear and one mononuclear complex were selected from the Cambridge Structural Database. The crystallographic structures and intermolecular interactions in the solid state were analyzed, and the effect of central metal ions was elucidated. The different contributions of the most numerous contacts were explained by examining additional ligands in the structure. Density functional theory (DFT) optimizations were performed for the selected complexes, and the applicability of different computational methods was discussed. The Quantum Theory of Atoms in Molecules (QTAIMs) approach was employed to identify and quantify interactions in nickel and vanadium complexes, highlighting the role of weak intermolecular interactions between ligands in stabilizing the overall structure. Molecular docking studies of the interaction between these complexes and Human Serum Albumin (HSA) demonstrated that all compounds bind within the active pocket of the protein. The overall size and presence of aromatic rings emerged as key factors in the formation of stabilizing interactions.

Keywords: 2-Hydroxy-3-methoxybenzaldehyde semicarbazone; DFT; Cambridge Structural Database; QTAIMs; molecular docking

check for updates

Academic Editors: Xiaoyan Li and Liuhua Mu

Received: 18 February 2025
Revised: 12 March 2025
Accepted: 17 March 2025
Published: 20 March 2025

Citation: Jevtovic, V.; Živković, J.M.; Rakić, A.A.; Alrashidi, A.A.; Alreshidi, M.A.; Alzahrani, E.A.; Alshammari, O.A.O.; Hussien, M.A.; Dimić, D. The Effect of Central Metal Ions (Dy, Er, Ni, and V) on the Structural and HSA-Binding Properties of 2-Hydroxy-3-methoxybenzaldehyde Semicarbazone Complexes. *Inorganics* **2025**, *13*, 95. https://doi.org/10.3390/inorganics13030095

Copyright: © 2025 by the authors. Licensee MDPI, Basel, Switzerland. This article is an open access article distributed under the terms and conditions of the Creative Commons Attribution (CC BY) license (https://creativecommons.org/licenses/by/4.0/).

1. Introduction

Semicarbazones, tridentate ONO Schiff bases, and derivatives of the general formula R-CH=N-NH-C(=O)-NH_2 are an important class of compounds obtained through the reaction of semicarbazides with aldehydes or ketones [1]. These compounds exhibit diverse coordination behavior, functioning as unidentate, bidentate, or multidentate chelating agents, depending on the structural characteristics of the parent aldehyde or ketone [2]. Semicarbazones' stability, chelating properties, and structural versatility have facilitated their extensive use in synthesizing transition metal complexes [3,4]. These complexes, often characterized by vivid coloration, are not only of chemical interest but also have

applications in analytical chemistry, including the detection and quantification of specific metal ions [5]. Beyond their chemical and analytical relevance, semicarbazones have gained significant attention for their diverse pharmacological properties. They exhibit a wide range of biological activities, including antitumoral, antibacterial, antiviral, antitrypanosomal, and antimalarial effects [4,6,7]. Moreover, coordination with metal ions has been shown to enhance their biological efficacy by improving lipophilicity, increasing activity, reducing side effects, and mitigating drug resistance. Notable examples include the complexes of Cu(II), Cr(III), Co(III), and dioxovanadium(V) [8–15]. The unique combination of chemical versatility and pharmacological potential underscores the importance of semicarbazones in fundamental research and applied sciences [16].

The ligand chosen for this contribution is 2-Hydroxy-3-methoxybenzaldehyde semicarbazone (HMBS) (Figure 1). This compound was prepared by the reaction between 2-hydroxy-3-methoxybenzaldehyde and semicarbazide hydrochloride, as described in the paper by Binil and coworkers in 2012 [17]. The following year, a dinickel(II) complex, with HMBS and 2,2′-bipyridine ligands, was obtained, and its crystallographic structure was solved by Vomisescu and coworkers [18]. Additionally, interesting structures with dioxovanadium(V) and palladium ions were presented in the references [6,19]. Schiff base ligands containing ONO multi-chelating systems have been incorporated into several lanthanide-based compounds [20–22]. Two of the phenoxo oxygen atoms of the HMBS ligand can act as a bridge between metal ions, leading to the conclusion that HMBS is a tetradentate ligand [23,24]. Li and coworkers described the crystallographic structures of three binuclear coordination compounds containing HMBS, dysprosium, and erbium central metal ions [24].

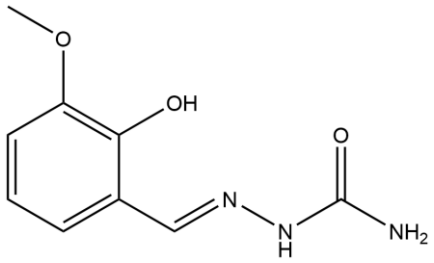


Figure 1. Chemical structure of 2-Hydroxy-3-methoxybenzaldehyde semicarbazone (HMBS).

The theoretical analysis of crystal structures often demands using a comprehensive repository of crystallographic data for small molecules and organic compounds, such as the Cambridge Structural Database (CSD) [25]. Tools within the CSD allow for statistical analysis, comparison of structural motifs, and identification of trends in bond lengths, angles, and non-covalent interactions [26–28]. This facilitates understanding structure–function relationships and aids in materials design and drug discovery. An additional useful method in the theoretical analysis of crystal structure is the Hirshfeld analysis [29]. This surface helps visualize and quantify interactions, such as hydrogen bonding, van der Waals forces, and π-π stacking. The study provides insights into crystal packing, interaction strengths, and contributions to overall stability, aiding in understanding material properties and molecular behavior in solid-state chemistry.

This contribution aims to present the crystallographic, quantum-mechanical, and Hirshfeld surface analysis of five transition metal complexes containing the 2-hydroxy-3-methoxybenzaldehyde semicarbazone ligand and four different metal ions (Dy, Er, Ni, and V), as shown in Figure 2. These structures were obtained from the Cambridge Structural Database (CSD) by searching for structures limited to mono and binuclear complexes containing HMBS ligands. Only those compounds with completely solved crystallographic

structures were selected for this article. The choice of metal ions is particularly important when structure, reactivity, and stability are concerned [30–32]. Special emphasis is given to the overall geometry of complex species in these examinations. The intramolecular interactions between donor atoms and central metal ions were assessed through the Quantum Theory of Atoms in Molecules (QTAIMs) approach for the selected complexes. A molecular docking study was used to investigate the potential binding affinities of complexes towards Human Serum Albumin (HSA).

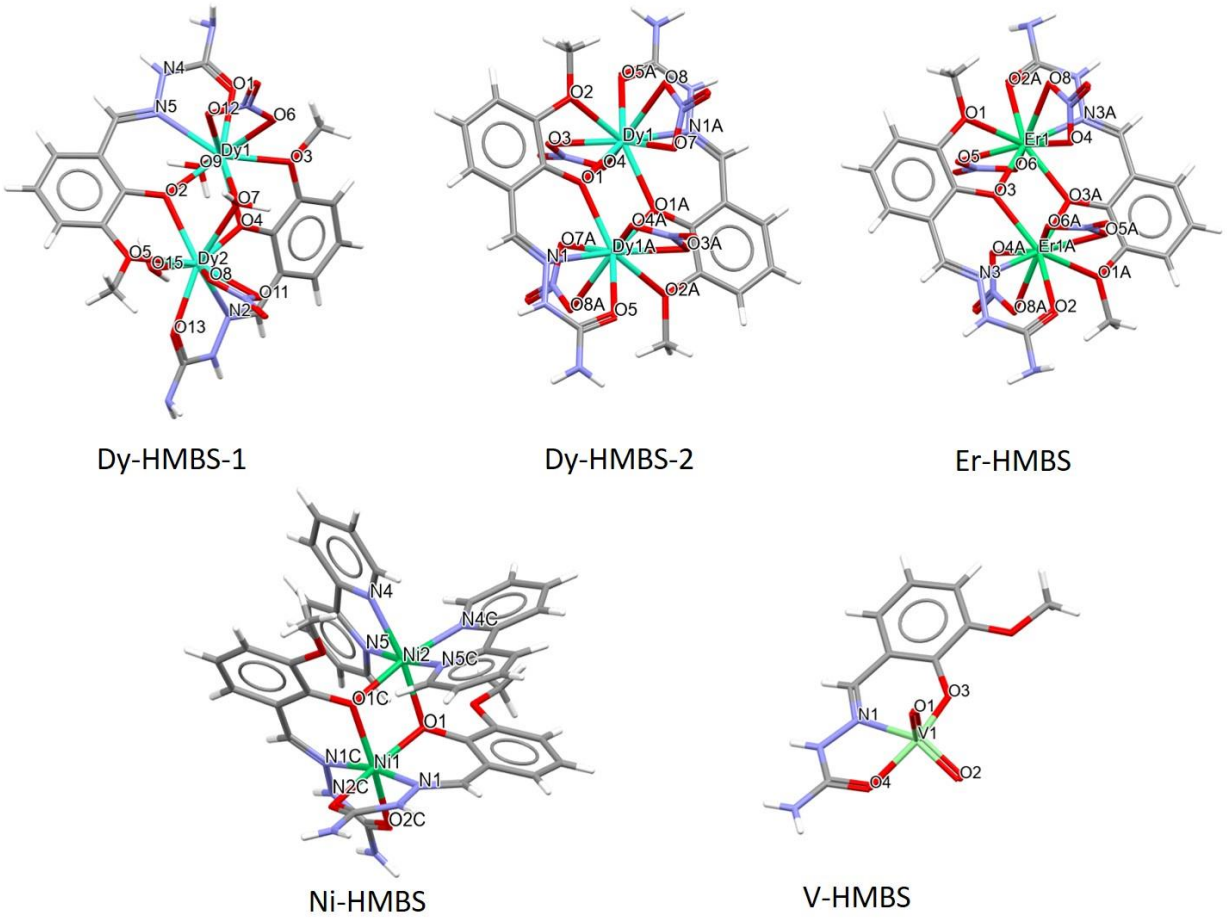


Figure 2. Crystallographic structures of the five complexes containing various metal ions and the HMBS ligand. The nitrogen atoms (N) are blue, the oxygen atoms (O) are red, the metal ions are green, the carbon atoms (C) are gray, and the hydrogen atoms (H) are white.

2. Results and Discussion

2.1. Crystallographic Structure of Selected Compounds

To analyze how different metal ions influence the coordination of the HMBS ligand, five complexes with varying metals and charges were selected from the Cambridge Structural Database (CSD) (Table 1). The leading search criteria included the presence of the HMBS ligand, and the results were limited to mono- and binuclear complexes. The crystal structures 1–4 belong to binuclear complexes with dysprosium, erbium, and nickel central metal ions, while structure 5 contains only vanadium(V) ions (Table 1). Although all complexes contain HMBS, other ligands and anions are present in the structure. The hydrogen atoms were placed within these structures in geometrically calculated positions, as outlined in the original references reporting examined complexes. In the structure of the **Dy-HMBS-1** complex, there are two dysprosium ions, surrounded by two HMBS ligands, three water molecules, and two nitrate ions (bidentate nitrato ligand). Each of the Dy(III) ions forms eight bonds in the coordination sphere. On the other side, structure **Dy-HMBS-2** contains

four bidentate nitrato ligands, although the rest of the structural features are the same. Coordinated nitrato ligands were also present in other lanthanide complexes, such as those described in reference [33]. The structure of the **Er-HMBS** is identical to the **Dy-HMBS-2**; only the central metal ion is changed. The tetradentate behavior of HMBS was observed for these three structures, as mentioned in the Introduction. In the structure containing nickel(II) ions, **Ni-HMBS**, one of the nickel ions, forms interactions with two HMBS ligands. However, these interactions are positioned between carbonyl oxygen, hydrazine nitrogen, and deprotonated phenyl oxygen atoms, as expected for this type of compound [34]. The simplest structure included in this study is denoted as **V-HMBS** and consists of the dioxovanadium(V) group and one HMBS ligand. Some of the fundamental properties of metal ions, geometry, and distances between characteristic atoms are presented in Table 1. The distances between central metal ions and oxygen/nitrogen atoms (d_{M-O} and d_{M-N}) are shown in Figure 3. The crystal packaging of complexes is given in Figures S4–S8.

Table 1. The REFCODE and other analyzed parameters for the different crystal structures with the HMBS ligand.

REFCODE	Notations	Metal Type	Oxidation State	Complex Charge	d_{M-O} (Å)	d_{M-N} (Å)	Space Group
BAKTOZ [24]	Dy-HMBS-1	Dy	+3	2+	2.278–2.293	2.506	P21/n
BAKTUF [24]	Dy-HMBS-2	Dy	+3	0	2.303–2.325	2.460	P-1
BAKVAN [24]	Er-HMBS	Er	+3	0	2.284–2.316	2.442	P-1
BEGSEO03 [18]	Ni-HMBS	Ni	+2	2+	2.032–2.090	2.015	Pbcn
GILQAV [6]	V-HMBS	V	+5	0	1.888–2.000	2.173	P21/c

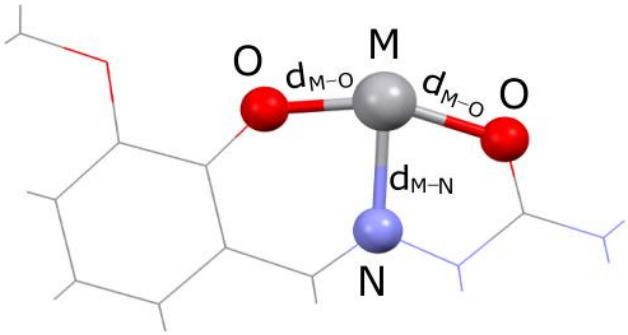


Figure 3. The d_{M-O} and d_{M-N} distances were analyzed in the metal complexes within the five crystal structures.

The triple-charged Dy(III) complex (**Dy-HMBS-1**) has a d_{M-N} distance (2.506 Å) slightly longer than the d_{M-O} distance (2.27–2.293 Å). In the neutral Dy(III) complex (**Dy-HMBS-2**), the d_{M-N} distance (2.460 Å) is also longer than the d_{M-O} distance (2.303–2.325 Å). The **Dy-HMBS-1** charged complex has slightly shorter d_{M-O} distances and a somewhat longer d_{M-N} distance than the neutral complex with the same metal ion. These values are similar, probably due to the repulsion between nitrato/aqua ligands and HMBS. The distance between the oxygen atom of the methoxy group and the Dy(III) ions is 2.405 Å, which is significantly higher than previously discussed. This atom participates in the formation of complex spheres, although it can be assumed that much stronger interactions are formed between phenyl oxygen and central metal ions. When the metal ion changes from Dy(III) to Er(III), as in the **Er-HMBS** crystal structure, the d_{M-N} and d_{M-O} distances decrease. In this neutral Er(III) complex, the d_{M-N} distance is 2.442 Å, while the d_{M-O} distances range from 2.032 to 2.090 Å. The same applies to interactions between the central metal ion and a methoxy oxygen atom (2.391 Å). This

reduction in bond lengths reflects the smaller ionic radius of Er(III) compared to Dy(III), as later discussed. Despite this, the trend of d_{M-N} distances being longer than d_{M-O} distances persists, similar to the Dy(III) complexes.

The doubly charged octahedral Ni(II) complex (**Ni-HMBS**) exhibits the shortest d_{M-O} and d_{M-N} distances among the analyzed binuclear complexes. In this structure, it is important to mention that the two HMBS ligands attached to one of the nickel(II) atoms are symmetrical. The second nickel atom is surrounded by two bipyridine ligands. The bond lengths between Ni(II) and the nitrogen atoms of this ligand are between 2.069 and 2.080 Å, similar to the same type of interactions between Ni(II) and HMBS. It can be proposed that these distances were shorter due to the absence of repulsive interactions between nitrato/aqua complexes and HMBS. Unlike the Dy(III) and Er(III) complexes, the Ni(II) complex shows a reversed trend, with the d_{M-N} distance (2.015 Å) being shorter than the d_{M-O} distance (2.032–2.090 Å). The neutral square pyramidal V(V) complex (**V-HMBS**) stands out, with the shortest d_{M-O} distances among all analyzed complexes, ranging from 1.888 to 2.000 Å. Its d_{M-N} distance, at 2.173 Å, is longer than the d_{M-O} distances, consistent with the observed trends in the Dy(III) and Er(III) complexes. The exceptionally short d_{M-O} distances in the V(V) complex are likely due to the high oxidation state of the vanadium ion, as well as the square pyramidal geometry of the mononuclear complex.

2.2. Hirshfeld Surface Analysis of Selected Compounds

Hirsfeld surface analysis is important in examining the intermolecular interactions within the crystallographic structures. Figure 4 presents the Hirshfeld surfaces of the investigated compounds, and the selected fingerprint plots for the most numerous contacts are presented in Figures S1–S3. Table 2 represents the percentages of the most numerous contacts. It is crucial to outline that only complex ions or neutral compounds are included in examining the formed interactions to determine structural effects.

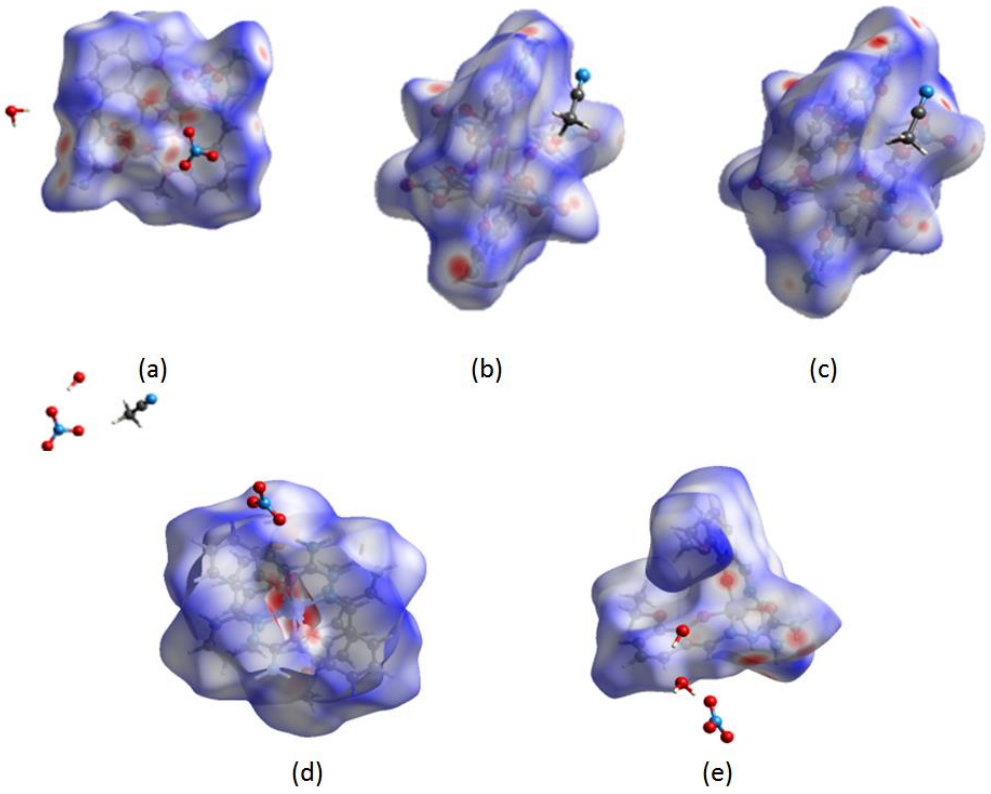


Figure 4. Hirshfeld surfaces of five examined complexes: (**a**) **Dy-HMBS-1**, (**b**) **Dy-HMBS-2**, (**c**) **Er-HMBS**, (**d**) **Ni-HMBS**, and (**e**) **V-HMBS**.

Table 2. The percentages of the most important contacts in the crystallographic structures were determined by Hirshfeld surface analysis.

Notation % Interactions	Dy-HMBS-1	Dy-HMBS-2	Er-HMBS	Ni-HMBS	V-HMBS
H···H	25.1	22.9	21.3	43.5	30.5
H···O	30.6	16.3	17.3	24.2	17.3
O···H	17.2	25.0	26.4	4.2	28.0
O···N	0.6	2.3	1.5	/	0.1
O···C	0.7	1.9	1.5	/	1.0
O···O	1.9	4.8	3.9	/	0.8
N···N	0.3	1.0	2.5	/	/
N···C	0.3	1.8	0.7	0.7	1.6
C···C	0.2	1.4	0.9	1.6	4.9

As previously discussed, the crystal structures **Dy-HMBS-1** and **Dy-HMBS-2** contain Dy(III) as the central metal ion but differ in their coordination environments and overall charge. In the **Dy-HMBS-1** structure, the Dy(III) complex cation is doubly positively charged, whereas in the **Dy-HMBS-2** crystal structure, the complex is neutral. This difference arises from additional coordinated three water molecules in the double-charged complex, along with the two nitrato and two HMBS ligands, compared to the neutral Dy(III) complex, which is coordinated by four nitrato groups and two HMBS ligands. These structural variations influence the types and percentages of intermolecular interactions in the two complexes. In the doubly charged Dy(III) complex, the proportion of H···O interactions is significantly higher, at 30.6%, compared to 16.3% in the neutral Dy(III) complex, as shown in Table 2 and Figure S2. This increase can be attributed to the coordinated water molecules, which provide additional hydrogen-bond donors, enhancing the formation of H···O interactions, as shown by dark red circles close to the electronegative groups. Conversely, the neutral Dy(III) complex exhibits a higher percentage of O···H interactions at 25.0% compared to 17.2% in the doubly charged complex. This discrepancy reflects the absence of coordinated water molecules in the neutral complex. Beyond hydrogen bonding, both Dy(III) complexes display substantial H···H interactions, indicative of van der Waals forces or packing effects. The doubly charged complex shows a slightly higher percentage of H···H contacts (25.1%) compared to the neutral complex (22.9%), suggesting that the charge and the presence of coordinated water molecules influence closer crystal packing.

Interestingly, the **Er-HMBS** crystal structure, which contains Er(III) as the central metal ion, has a similar coordination environment to the neutral Dy(III) complex in the **Dy-HMBS-2** crystal structure (Table 1). As a result, the percentages of various intermolecular interactions in **Er-HMBS** are nearly identical to those observed in **Dy-HMBS-2**, as noted in Table 2. This reinforces the idea that the coordination environment is pivotal in determining the interaction profile, irrespective of the specific metal ion involved. This result is consistent with findings from the study conducted by Harraf and coworkers, in which Pr(III), Sm(III), Gd(III), Dy(III), and Ho(III) complexes with ligands derived from 4-aminoantipyrine were examined. The relative percentages of the most numerous contacts were the same across this series of complexes with similar structures [35]. The **Ni-HMBS** crystal structure, containing Ni(II) as the central metal ion, exhibits the highest percentage of H···H interactions among the analyzed structures (Table 2). This is attributed to aromatic bipyridine and two HBMS ligands that enclose the central metal ion and point outward with hydrogen-rich groups. The number of polar groups in the ligands around nickel(II) is much lower than that of the other examined complexes. The units in crystal packaging of the Ni-HMBS complex are closer compared to other complexes (Figure S6). This arrangement introduces more extensive van der Waals interactions than the ligands in

the Dy(III) and Er(III) complexes. Additionally, the Ni(II) complex shows a relatively high percentage of H···O interactions (24.2%) due to the specific arrangement of its ligands, as shown in Figure 4, in the vicinity of the nitrate counterion. Finally, the **V-HMBS** crystal structure, which features a V(V) complex, demonstrates the high percentage of H···H interactions (30.5%) (Table 2). This is probably a result of its compact packing. Notably, the two oxygen atoms directly coordinated to the V(V) ion contribute to a larger percentage of O···H interactions compared to the other complexes.

Other interactions involving electronegative O and N atoms, such as O···N, O···C, O···O, N···N, and N···C, generally occur at levels below 2% in most of the analyzed crystal structures. However, there are some exceptions. In the **Dy-HMBS** and **Er-HMBS** crystal structures, O···O interactions are more pronounced, reaching 4.8% and 3.9%, respectively, due to the coordination of four nitrato groups to two metal ions. Another significant exception is found in the **V-HMBS** crystal structure, where C···C interactions account for 4.9%, indicating a close crystal packing. Additionally, the influence of co-crystalized solvent molecules cannot be neglected, as it is important for the stabilization interactions and solid-state assembly of molecules, as discussed in reference [36].

2.3. DFT Optimization of Structure

A comparative analysis was conducted between the crystallographic structures and their corresponding optimized geometries to assess the reliability of the optimized structures. Due to the differences in the electronic structure of central metal ions, different basis sets were applied in conjunction with the B3LYP method. The non-metallic atoms were optimized using the 6-31+G(d,p) basis set, while the basis sets for vanadium/nickel (def2-TZVP) and erbium (Stuttgart 1997 ECP) were obtained from the Basis Set Exchange. Due to their complexity, the compounds containing dysprosium ions were omitted from this study. The comparison was performed using two statistical parameters: the correlation coefficient (R) and the mean absolute error (MAE). The MAE represents the average absolute difference between the crystallographic and optimized structural parameters, providing a quantitative measure of deviation. The comparison of bond distances and bond angles was carried out for three representative complexes: **Er-HMBS** (Tables S1 and S2), **Ni-HMBS** (Tables S3 and S4), and **V-HMBS** (Tables S5 and S6), with the atomic enumeration of atoms shown in Figures S9–S11. For the experimental errors for the bond lengths and angles, see references [6,18,24]. When bond lengths are considered, the R values are 0.997 (**Er-HMBS**), 0.959 (**Ni-HMBS**), and 0.994 (**V-HMBS**), with the MAE values range from 0.028 to 0.037 Å. On the other side, the R values for the bond angles are 0.993 (**Er-HMBS**), 0.931 (**Ni-HMBS**), and 0.978 (**V-HMBS**), while the MAE values are approximately 2°. The lowest R and highest MAE values were calculated for **Ni-HMBS**, as this complex's octahedral geometry around the central metal ion involved the interaction of one oxygen atom and two nickel(II) ions. Due to the optimization in a vacuum, the geometry was slightly disordered. Notably, after optimization in a vacuum, significant elongation of the Ni2–O3 and Ni2–N12 bond distances in Ni-HMBS was observed (Table S3) compared to the experimental crystal structure, which was determined in a polar solvent environment. To prevent bias in the statistical analysis, these bond distances were excluded from the calculations of the R and the MAE. The results indicate a strong correlation between theoretical and crystallographic structures, as reflected by the correlation coefficient values ($R \approx 1$), signifying that the optimized geometries closely resemble their experimental counterparts. The MAE values for bond distances and angles were comparable across all three complexes. However, the MAE for bond angles was proportionally higher than the bond distances, likely due to the inherent flexibility of angular parameters in the absence of solvent effects or intermolecular interactions present in the crystal lattice.

Given the high structural agreement between the experimental and optimized geometries, further molecular docking studies were conducted using the crystallographic structures without additional geometry optimization. This decision was based on the observation that, despite its computational cost, geometry optimization did not introduce significant structural differences that would impact docking results. By preserving the experimental structures, computational resources were allocated efficiently without compromising the accuracy of docking simulations.

2.4. QTAIMs Analysis

QTAIMs analysis is a valuable technique to access the type and strength of intramolecular interactions within the optimized structures of transition metal complexes [37,38]. The complexes **Ni-HMBS** and **V-HMBS** were selected for this analysis as they do not contain additional species that could influence the geometry and stability of the interactions between the central metal ion and the ligand. This analysis examines Bond Critical Points (BCPs) between interacting atoms. Bader and Essen proposed a classification of interactions, which includes the values of electron density and the Laplacian. The first type of interaction includes covalent interactions with a high electron density value. The second type of interactions are ionic bonds, van der Waals interactions, and hydrogen bonds with electron density lower than 0.001 a.u. [39,40]. These parameters, together with Lagrangian kinetic electron energy (G(r)), potential electron energy (V(r)), the density of total electron energy (H(r) = G(r) + H(r)), and the interatomic bond energy (E_{bond} = V(r)/2) [41], for the metal-donor atoms in the complexes, are given in Table S7.

These intramolecular interactions were first followed for the simplest complex compound with vanadium(V), as seen in Table S7. The highest electron density value was found for V=O bonds (0.273 and 0.276 a.u.), followed by the highest value of the Laplacian (0.924 and 0.933 a.u.). This result was expected, as these were the shortest bonds and the core of the optimized molecule. The interaction strength between donor atoms of HMBS and V(V) depends on their positions, as evident in V−O bonds. The bond between the phenolic oxygen atom and central metal ion has an electron density of 0.106 a.u. In contrast, the carbonyl oxygen and vanadium(V) bond has an electron density of 0.059 a.u. This result also proves the importance of the phenolic group and extended delocalization in the formation of interactions between the donor atom and central metal ion. The hydrazine nitrogen also interacts with vanadium through interactions with an electron density of 0.049 a.u. A more detailed classification of interactions can be found in the research by Bianchi and coworkers, and it depends on the relative ratio of G(r) and V(r). Based on this classification, covalent bonds have a –G(r)/V(r) ratio lower than 1 and the intermediate (transit) region exists between the values of 1 and 2, while ionic bonds and van der Waals interactions have a value for this parameter higher than 2. According to these values, interactions between oxygen atoms in V=O and phenolic oxygen have the highest covalent contribution, while the other two bonds lay in the transient region. Additional proof for this statement is obtained when values of the total electron density are observed. Bonds with negative H(r) value can be classified as partially covalent (V=O and V−O_{phen}) [41]. The interaction energy, calculated as the half value of V(r), as proposed by Espinosa, is also shown for the interactions. These values nicely follow the previous discussion. The interatomic bond energies for dioxovanadium(V) species are −818.0 and −805.4 kJ mol^{-1}. Much lower energies were calculated for V−O_{phen} (−203.4 kJ mol^{-1}), V−O_{carb} (−89.3 kJ mol^{-1}), and V−N_{hydr} (−65.0 kJ mol^{-1}).

As previously explained in detail, the structure of the **Ni-HMBS** complex contains two nickel ions in different environments. The first nickel(II) ion is surrounded by two HMBS ligands. In this structure, the highest electron densities were found between hydrazine nitrogen atoms and Ni(II) (0.106 and 0.089 a.u.). The bonds are characterized by a partial

covalent character, as evident from the negative values of the total electron density and the –G(r)/V(r) ratio. The asymmetric positioning of the two HMBS ligands leads to different values for the interatomic energies of −279.3 and −193.1 kJ mol^{-1}. The optimization of the structures results in the elongation of certain bonds due to the absence of counterions in the crystallographic structure. This can be seen in Ni−O_{phen} bonds, with electron densities of 0.020 and 0.106 a.u and interatomic bond energies of −22.7 and −251.3 a.u. Nevertheless, the partial covalent character of these bonds is preserved (-G(r)/V(r) = 0.9). The interactions between the central metal ion and the carbonyl oxygen atoms are generally the weakest when donor atoms within one HMBS ligand are compared. These bonds are characterized by interatomic bond energies of −31.4 and −194.4 kJ mol^{-1}. Additional stabilization of the nickel(II)–HMBS structure is formed through a bridging interaction between carbonyl oxygen atoms of HMBS and two nickel ions. One of these interactions, denoted as Ni2−$O_{phen,1}$, has an electron density of 0.092 a.u., a partial covalent character (negative H(r)) value, and an interatomic bond energy of −202.4 kJ mol^{-1}. The second interaction of this type was not observed in the QTAIMs analysis due to the system's relaxation. The second nickel(II) ion is surrounded by four nitrogen atoms from biphenyl ligands. These interactions, denoted as Ni−N, have electron densities between 0.31 and 0.099 a.u. Again, a wide range of values was obtained due to slight distortion of the system, which led to interatomic bond energies of −36.7 a.u. for one of the interactions and around −200.0 kJ mol^{-1} for the other three. In general, the interaction energies formed between donor atoms and vanadium(V) were lower compared to nickel(II), probably due to the presence of two oxygen atoms coordinated directly to this central metal ion. Differences in interaction strengths were observed in the Mn(II), Co(II), and Cu(II) complexes with 2-furaldehyde semicarbazone [42].

The structure of the second complex is stabilized by several weak interactions that are important for the overall stability of the complex. They originate from several electronegative atoms in the structures of HMBS and bipyridine ligands. As presented in Table S7, the most numerous interactions are formed between bipyridine and HMBS moieties. The strongest interactions were found between oxygen atoms attached to HMBS's phenyl ring and bipyridine hydrogen atoms, with interaction energies of −17.4, −13.7, −9.1, and −8.1 kJ mol^{-1}. These interactions belong to the transient region with a -G(r)/V(r) ratio equal to or higher than 1 and a positive total electron density. The hydrazine nitrogen atom of HMBS interacts with the hydrogen atom of bipyridine with an interaction energy of −3.6 kJ mol^{-1}. An additional type of interaction exists between the oxygen atom of HMBS and the nitrogen atom of pyridine, although it is much weaker than the previously mentioned classical hydrogen bonds. A similar interaction energy was calculated for the N···C interaction between the two ligands (−3.6 kJ mol^{-1}). A weak hydrogen bond between the carbon atom of bipyridine and HMBS is an example of another type of interaction, although much weaker than those that include electronegative atoms. Intramolecular interactions between hydrogen atoms within bipyridine also contribute to the overall stability (−7.9 kJ mol^{-1}). This analysis proved that interactions within the crystallographic structures were important for stabilizing the structure, and they explain why the overall geometry of the complex is significant for the activity towards proteins, as described in the following section.

2.5. Molecular Docking Analysis of HSA Binding Properties

2.5.1. Docking Calculations and Binding Site Determination

In the initial docking iteration, the complexes were examined across the entire volume of the HSA protein. The results indicated a preferential binding site near the amino acid Trp214 (Figure S12), suggesting that all the complexes could quench HSA fluorescence in

spectrofluorimetric measurements. To improve computational efficiency while maintaining accuracy, subsequent docking calculations were refined by restricting the search space to a smaller region, using the same level of theory. The docking box was constructed to encompass binding sites surrounding Trp214, specifically FA7, FA8, and FA9. Figure S7 illustrates these binding domains and subdomains. Among the investigated complexes, the square pyramidal vanadium complex exhibited the closest proximity to Trp214. However, due to steric effects, all four voluminous binuclear complexes were localized to the same binding region, which was not in the immediate vicinity of Trp214 (Figure 5a).

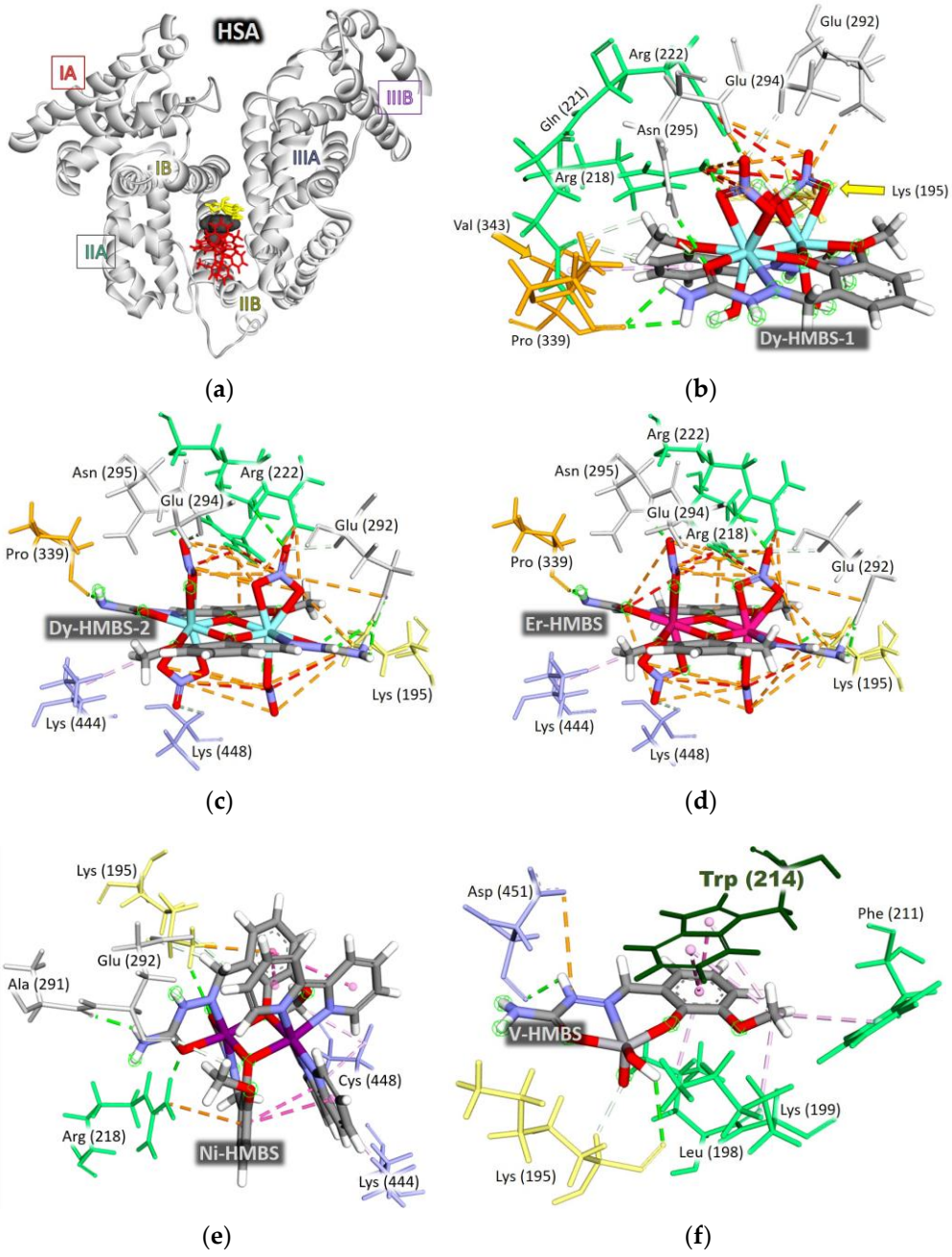


Figure 5. (**a**) The positions of the complexes inside the HSA structure. The interactions of the complexes with the amino acids in the FA8 binding site, (**b**) **Dy-HMBS-1**, (**c**) **Dy-HMBS-2**, (**d**) **Er-HMBS**, (**e**) **Ni-HMBS**, and (**f**) **V-HMBS**. The dashed lines indicate the different types of intermolecular interactions, with colors representing the following: orange—attractive charge, salt bridge, or π-cation interaction; green—conventional hydrogen bond; light green—carbon–hydrogen bond; pink—π-π stacking; baby pink—π-alkyl; red—unfavorable positive–positive interaction.

2.5.2. Binding Energies and Structural Considerations

Table 3 summarizes the data concerning the details of the complexes without counterions, including structural information and changes in the Gibbs free energy of binding (ΔG_b) values. The smallest complex, **V-HMBS**, which features a single aromatic ring in its HMBS structure, exhibited the lowest change in the Gibbs free energy of binding (-29.54 kJ mol^{-1}). Its simple square pyramidal geometry allows access to sterically hindered regions of HSA, while simultaneously limiting interaction possibilities. The most voluminous complex, **Ni-HMBS**, which contains ligands with six aromatic rings, displayed a binding energy nearly equivalent to **V-HMBS** (-29.37 kJ mol^{-1}). While these values are lower than those of the other three complexes, they remain in the higher part of the range, between 18 and 34 kJ mol^{-1} [34,43–45], obtained from the literature values for similar pyridoxal semicarbazone-based complexes.

Interestingly, neither the size, type, nor valence of the central metal ion significantly influenced the binding energy. Instead, the presence of NO_3^- ligands appeared to play a decisive role. The complexes containing nitrato ligands exhibited significantly higher absolute binding energies, exceeding 37 kJ mol^{-1}. Notably, the binding free energy showed a strong dependence on the presence of these ligands, suggesting that NO_3^- anions contribute substantially to the strength of the interactions. In the experimental study by Papadopoulos and coworkers, copper(II) complexes with 5–fluoro–salicylaldehyde containing nitrato ligands had higher binding constants towards BSA than complexes with chlorido ligands [46].

Table 3. Structural information and changes in Gibbs free binding energies.

No.	Ligand	CMI	CN	R(CMI) (pm)	The Structure Used for Docking	ΔG_b (kJ mol^{-1})
1	**Dy-HMBS-1**	2Dy(+3)	9	122.3 CR	$[Dy_2(HMBS)_2(NO_3)_2(H_2O)_3]^{2+}$	−37.07
2	**Dy-HMBS-2**	2Dy(+3)	9	122.3 CR	$[Dy_2(HMBSs)_2(NO_3)_4]$	−44.35
3	**Er-HMBS**	2Er(+3)	9	106.2 IR	$[Er_2(HMBS)_2(NO_3)_4]$	−43.60
4	**Ni-HMBS**	2Ni(+2)	6	83.0 CR	$[Ni_2(HMBS)_2(bpy)_2]^{2+}$	−29.37
5	**V-HMBS**	V(+5)	5	46.0 IR	$[VO_2(HMBS)]$	−29.54

The coefficient **2** in front of the central metal ion (CMI) indicates that the complex is binuclear. **CN** represents the coordination number, **R(CMI)** denotes the ionic radius of the central metal ion in the low-spin (ls) state [47], **CR** refers to the crystal radius when the crystal structure is used for docking calculations, and **IR** corresponds to the effective ionic radius when the optimized structures are employed for docking studies. **bpy** stands for the bipyridine ligand, while **HMBS** represents the hydroxy-3-methoxybenzaldehyde semicarbazone ligand. **ΔGb** refers to the theoretically calculated change in the Gibbs free energy of binding.

2.5.3. Interaction Patterns and Binding Site Specificity

Previous studies have demonstrated that metal complexes containing HMBS preferentially bind to the FA8 site. The steric effect confines bulky complexes to the periphery of the FA8 binding region. In complexes incorporating NO_3^- ions, the HMBS ligand positions the central metal ion in a planar arrangement, while the nitrato ligands extend above and below this plane. This orientation exposes ions to the surrounding polar and charged amino acids at the FA8 binding site's edge. Each NO_3^- ion participates in an average of eight strong electrostatic and hydrogen bond interactions.

Repulsive interactions were also identified, averaging one or two per NO_3^- ion. Specifically, NO_3^- ions exhibited repulsive interactions with positively charged amino acid groups, including -NH_3 (Lys195) and -$C(NH_2)_2$ (Arg218, Arg222). However, Arg218 also demonstrated electrostatic attraction to the benzene π-electron system of the HMBS ligand. Additionally, the NH_2 and NH groups of HMBS occasionally formed hydrogen bonds with the carboxyl and carbonyl groups of Glu292 and Pro339, respectively. Notably, a single repulsive interaction involving an NH group of the chelating ligand occurred exclusively in the **Er-HMBS** complex when it approached the -$C(NH_2)_2$ group of Arg218.

In the **Dy-HMBS-1**, **Dy-HMBS-2**, and **Er-HMBS** complexes, nitrato ligands formed an extensive network of strong electrostatic attractions among themselves and with the surrounding amino acids, effectively neutralizing the influence of a few repulsive interactions. The amino acids Lys195, Arg218, and Arg222 are characterized by their strong tendency to form electrostatic interactions with NO_3^- ions due to the presence of the $-C(NH_2)_2^+$ and $-NH_3^+$ charged groups. The NH and CH groups allow them to participate in hydrogen bonding with NO_3^-, however, hydrogen bonding is more characteristic of Asn295, Glu294, and Glu292. NO_3^- ions acted as electrostatic shields for the remainder of the complexes. This shielding effect was so pronounced that only the N-H group of the ligand in **Dy-HMBS-1** successfully engaged in an attractive electrostatic interaction with the carboxyl group of Glu292, facilitated by the simultaneous hydrogen bonding of Glu292 with a neighboring NH_2 group. Hydrogen bonding interactions were also observed between heteroatoms in the HMBS ligand and amino acid residues, including Asn295 (amine N-H group), Pro339 (C=O group), Lys295 (NH_3 group), Arg218 (NH_2 group), and Glu292 (C=O group). Weaker carbon-hydrogen bonding interactions involved Glu292, Glu294, Glu221, and Cys448. Notably, the presence of NO_3^- ions suppressed hydrophobic interactions, which dominated in complexes lacking NO_3^-, such as **Ni-HMBS** and **V-HMBS**.

2.5.4. Hydrophobic Interactions in Non-Nitrate Complexes

Hydrophobic interactions were predominantly observed in the **Ni-HMBS** and **V-HMBS** complexes, where the benzene π-system played a key role in π-π stacking and π-alkyl interactions. Lys444 and Lys448 were identified as key residues for these interactions. In the **Dy-HMBS-2** and **Ni-HMBS** complexes, only a prominent CH_3 group successfully formed an alkyl–alkyl interaction with Lys444.

V-HMBS exhibited distinct behavior due to its unique structural features. While its benzene and methyl groups contributed to hydrophobic interactions, the presence of two polar groups with heteroatoms introduced additional interaction possibilities. The hydrophobic region formed π-π stacking, π-alkyl, and alkyl–alkyl interactions with Phe211, Trp214, and Lys199. Aqueous ligands participated in hydrogen bonding with Lys195, while the N-H group engaged in hydrogen bonding and electrostatic attractions with Asp451.

2.5.5. Intramolecular Interactions and Structural Stability

In addition to intermolecular interactions, numerous intramolecular interactions were identified, playing a crucial role in complex stability. In the **Dy-HMBS-2** and **Ni-HMBS** complexes, repulsive interactions between neighboring NO_3^- ions were counterbalanced by a predominant number of attractive interactions, stabilizing the complex structure. In contrast, intramolecular interactions between NO_3^- ions in **Dy-HMBS-1** were not observed due to the presence of a water molecule between them. The primary stabilizing factor in **Dy-HMBS-1** was the coordination bonding between ligands and two Dy(III) ions.

Electrostatic intramolecular interactions, hydrogen bonds, and hydrophobic interactions varied depending on the ionic radius of the central metal ion, the number and type of ligands, and their spatial orientation. The Dy^{3+} ion, with a high crystal radius (122.3 pm [1]), prevented intramolecular interactions between axially oriented NO_3^- ions and two equatorial HMBS ligands in the **Dy-HMBS-1** and **Dy-HMBS-2** complexes. In contrast, Er^{3+}, with a significantly lower effective ionic radius (106.2 pm), engaged in electrostatic interactions between NO_3^- ions and the $N\text{-}H^+$ groups of the chelating ring in **Er-HMBS**.

The Ni^{2+} ion, with a low crystal radius (83 pm), facilitated intramolecular π-π stacking interactions within the **Ni-HMBS** complex due to parallel ligand orientation. Conversely, the V^{5+} ion, possessing the smallest effective ionic radius (48 pm), did not form intramolec-

ular interactions due to ligand positioning. The experimental and theoretical coordination bond lengths (Tables S8–S11) correlated well with the ionic radii. The Dy^{3+}-NO_3^- coordination bonds in **Dy-HMBS-1** and **Dy-HMBS-2** measured approximately ~2.5 Å, whereas the Er^{3+}-NO_3^- distances averaged 2.4 Å. The Ni^{2+} coordination distances in **Ni-HMBS** were around 2.1 Å, while the V^{5+}-O^{2-} bond lengths were even shorter, averaging 1.6 Å.

3. Materials and Methods

3.1. Cambridge Structural Database (CSD) Search

To select complexes for analysis, a search in the Cambridge Structural Database (CSD (November 2020 release, version 5.42)) [48] was conducted for various metal complexes with the 2-Hydroxy-3-methoxybenzaldehyde semicarbazone ligand. A CSD search was performed using the ConQuest 2021.2.0 program [49], satisfying the following criteria: (a) a crystallographic R factor below 10%, (b) error-free coordinates, and (c) no polymer structures. The structures were visualized by using Mercury v 3.0 [50]. For further analysis, five structures with different metals and charges were selected.

3.2. Hirshfeld Surface Analysis

The intermolecular interactions in the crystallographic structure are crucial in determining its properties. In this study, the CrystalExplorer program [51] was employed for Hirshfeld surface analysis. The interactions were visualized using a graphical representation of two distances: d_e, the distance to the nearest nucleus outside the surface, and d_i, the distance to the nearest nucleus inside the surface [29,52]. These points were colored by comparing the van der Waals separation between nuclei. The normalized distances for BAKTOZ, BAKTUF, BAKVAN, BEGSE03, and the GILQAV crystal structures were between −0.7099 (red) and 1.4918 (blue), −0.3852 (red) and 1.3848 (blue), −0.2003 (red) and 1.3830 (blue), −0.6970 (red) and 1.6551 (blue), and −0.6034 (red) and 1.7615 (blue), respectively. The fingerprint plots for the selected interactions are given as the Supplementary Material.

3.3. Optimization of Structures and QTAIMs Analysis

The crystallographic structures of the selected complexes were optimized in the Gaussian 09 Program package [53]. The two complexes containing dysprosium ions were omitted from the quantum chemical calculations due to the size of the metal ion and surrounding ligand system. For the remaining complexes, the B3LYP functional was used. The non-metallic atoms were optimized using a 6-311++G(d,p) basis set [54]. On the other hand, two different basis sets were applied for the vanadium/nickel (def2-TZVP) [55,56] and erbium (Stuttgart 1997 ECP) [57], as found on the Basis Set Exchange [58,59]. The latter basis set, with relativistic effective core potential (ECP), was selected due to the size of the erbium ion. The optimizations were performed without any geometrical constraints for the separated complex species, and the absence of imaginary frequencies proved that minima on the potential energy surface were obtained. The chosen theoretical framework ensures a reliable description of molecular interactions, coordination environments, and electronic properties, which are essential in understanding binding affinities and reaction mechanisms. The optimized and crystallographic structures were compared using the correlation coefficient (R) and the mean absolute error (MAE). The stabilization interactions between the central metal ions and surrounding ligands were examined and discussed through the Quantum Theory of Atoms in Molecules (QTAIMs) approach, as proposed by Bader [60,61]. These calculations were performed in the AIMAll [62] program package, starting from the .wfx file obtained in the Gaussian 09.

3.4. Molecular Docking

Molecular docking plays a crucial role in understanding the binding mechanisms of small molecules to biomacromolecules, providing insights into the key interactions that govern stability and affinity. This study investigated the binding interactions of five structurally diverse metal complexes with human serum albumin (HSA, PIB ID:2bxd [63]). The selected complexes differ in the type and oxidation state of the central metal ion, with at least one HMBS ligand present in each system. In contrast, the remaining ligands vary in size, charge, and chemical nature. These variations result in distinct molecular architectures, ranging from the square pyramidal **V-HMBS** complex [6], which contains a single aromatic ring, to the bulky three-dimensional **Ni-HMBS** complex [18], which features six aromatic rings. Other complexes include **Dy-HMBS-1**, **Dy-HMBS-2**, and Er-HMBS [24]. The primary objective of this study is to elucidate how molecular size, spatial arrangement, metal coordination environment, ligand diversity, and overall charge influence the binding affinity and interaction pattern with HSA. To achieve this, docking calculations were performed to assess three key aspects of molecular recognition: the Gibbs free energy of binding, preferred binding sites, and intermolecular interactions. Molecular docking simulations were conducted using AutoDock 4.2.6 [64], as implemented in the AMDock software package (version 1.5.2) [65]. Two sets of docking calculations were performed. The first set explored the entire HSA protein to identify potential binding sites, while the second set focused on a localized region surrounding the Trp214 residue, specifically investigating the FA7, FA8, and FA9 binding sites. The docking protocol employed the AMBER force field, with an exhaustiveness parameter set to enhance conformational sampling. Each simulation generated ten poses per complex, with 250,000 energy evaluations and ten independent runs. The clustering tolerance was set to 2 Å to ensure a rigorous analysis of the binding modes. This computational approach enables a comprehensive assessment of the factors governing the interaction of metal complexes with HSA, providing valuable insights into their potential bioavailability, transport, and pharmacological relevance.

4. Conclusions

Five complex compounds containing 1-(2-hydroxy-3-methoxybenzylidene)-semicarbazide ligand and dysprosium, erbium, nickel, and vanadium central metal ions were examined. The differences in the coordination abilities, especially in terms of the coordination bond number of central metal ions, are crucial in determining the geometry and stability. The analysis of crystallographic parameters in the first line showed the bond lengths between the oxygen/nitrogen atoms of HBMS and metal ions and the importance of the ionic radius and overall charge of the complex species. The variation in the metal–ligand distances across these complexes underscores the influence of the metal ion's size, charge, and oxidation state on the coordination geometry. For the same metal ion (Dy(III)), the charge had a significant effect, with the doubly charged **Dy-HMBS-1** complex showing stronger oxygen coordination than the neutral **Dy-HMBS-2** complex. Bond distances generally decrease when transitioning to smaller metal ions, such as Er(III), or to higher oxidation states, such as V(V). The Ni(II) complex deviated from this pattern, reflecting the influence of the coordination environment. These findings highlight the intricate balance between electronic and steric factors in determining coordination behavior and provide some insights for designing metal–ligand systems. Additionally, auxiliary ligands, such as nitrato, aqua, and bipyridil, were essential in determining the overall geometry and the predominant intermolecular contacts of the complexes within the crystal structures. The nitrato ligands increased the amount of O···H to 25%, similar to the contribution of oxygen atoms in the dioxovanadium(V) moiety. Computational studies demonstrated that the selected theory has sufficient accuracy in reproducing experimental bond lengths

and angles, yielding high correlation coefficients and low mean absolute errors when comparing crystallographic and optimized parameters. The QTAIMs analysis further revealed that interaction strength depended on the positioning of donor atoms, while weak intramolecular interactions significantly contributed to the overall stability of the complex. The interaction energies were higher in the case of Ni-HMBS than V-HMBS, due to the presence of oxygen atoms in the dioxovanadium(V) moiety. Molecular docking studies elucidated the key role of intermolecular interactions in binding metal complexes to human serum albumin (HSA). The spatial dimensions of the complexes dictated their binding preferences. Large 3D complexes were associated with the edge of the FA8 region, whereas the vanadium complex with planar HBMS and tiny oxygen ligands, benefiting from reduced steric hindrance, accesses the confined space above Trp214. The changes in Gibbs free binding energy ranged from -30 to -45 kJ mol^{-1}. These anions played a fundamental role in stabilizing the complexes through strong electrostatic interactions, which prevailed over the hydrogen bonding and hydrophobic effects. Additionally, nitrato ligands act as electrostatic shields, mitigating repulsive interactions and enhancing the structural integrity of the complexes within HSA. In contrast, complexes devoid of NO_3^- ligands rely predominantly on hydrophobic interactions for stabilization. These findings highlight the significance of electrostatic forces in dictating the stability and positioning of the metal complexes in biological macromolecules. The insights gained from this study contribute to the rational design of metal-based drugs and biomolecular probes, providing a foundation for future developments in medicinal and bioinorganic chemistry.

Supplementary Materials: The following supporting information can be downloaded at: https://www.mdpi.com/article/10.3390/inorganics13030095/s1. Figure S1: the fingerprint plots for H···H contacts within the structures: (a) **Dy-HMBS-1**, (b) **Dy-HMBS-2**, (c) **Er-HMBS**, (d) **Ni-HMBS**, and (e) **V-HMBS**; Figure S2: the fingerprint plots for H···O contacts within the structures: (a) **Dy-HMBS-1**, (b) **Dy-HMBS-2**, (c) **Er-HMBS**, (d) **Ni-HMBS**, and (e) **V-HMBS**; Figure S3: the fingerprint plots for O···H contacts within the structures: (a) **Dy-HMBS-1**, (b) **Dy-HMBS-2**, (c) **Er-HMBS**, (d) **Ni-HMBS**, and (e) **V-HMBS**; **Figure S4**: the crystal packaging of **Dy-HMBS-1**; Figure S5: the crystal packaging of **Dy-HMBS-2**; Figure S6: the crystal packaging of **Er-HMBS**; Figure S7: the crystal packaging of **Ni-HMBS**; Figure S8: the crystal packaging of **V-HMBS**; Table S1: the experimental and theoretical (ub3lyp/6-31+G(d,p)(H,C,N,O)/SDD(Er) level of theory) bond lengths (in Å) of tetrakis(nitrato)-bis(μ-2-[(2-carbamoylhydrazinylidene)methyl]-6-methoxyphenolato)-di-erbium acetonitrile solvate (CSD Refcode: BAKVAN); Table S2: the experimental and theoretical (ub3lyp/6-31+G(d,p)(H,C,N,O)/SDD(Er) level of theory) bond angles (in °) of tetrakis(nitrato)-bis(μ-2[(2-carbamoylhydrazinylidene)methyl]-6-methoxyphenolato)-di-erbium acetonitrile solvate (CSD Refcode: BAKVAN); Table S3: the experimental and theoretical (ub3lyp/6-31+G(d,p)(H,C,N,O)/def2-TZVP(Ni) level of theory) bond lengths (in Å) of bis(μ-2- ((2-oxido-3-methoxyphenyl)methylidene)hydrazine-1-carboxamidato)-bis(2,2′-bipyridine)-di-nickel(II) dinitrate (CSD Refcode: BEGSEO03); Table S4: the experimental and theoretical (ub3lyp/6-31+G(d,p)(H,C,N,O)/def2-TZVP(Ni) level of theory) bond angles (in °) of bis(μ-2-((2-oxido-3-methoxyphenyl)methylidene)hydrazine-1-carboxamidato)-bis(2,2′-bipyridine)-di-nickel(II) dinitrate (CSD Refcode: BEGSEO03); Table S5: the experimental and theoretical (ub3lyp/6-31+G(d,p)(H,C,N,O)/def2-TZVP(V) level of theory) bond lengths (in Å) of (2-(2-Oxido-3-methoxybenzylidene)hydrazinecarboxamidato)-dioxo-vanadium(v) ethanol solvate (CSD Refcode: GILQAV); Table S6: the experimental and theoretical (ub3lyp/6-31+G(d,p)(H,C,N,O)/def2-TZVP(V) level of theory) bond angles (in °) of (2-(2-Oxido-3-methoxybenzylidene)hydrazinecarboxamidato)-dioxo-vanadium(V) ethanol solvate (CSD Refcode: GILQAV); Figure S9: the optimized structure of **Er-HMBS** in a ball-and-stick representation, with the assigned atom symbols and corresponding serial numbers; Figure S10: the optimized structure of **Ni-HMBS** in a ball-and-stick representation, with the assigned atom symbols and corresponding serial numbers; Figure S11: the optimized structure of V-HMBS in a ball-and-stick representation, with the assigned atom symbols and corresponding serial numbers; Table S7: the calculated Bond Critical Points (BCPs) properties: the electron density

($\rho(r)$) and its Laplacian ($\nabla^2\rho(r)$); the Lagrangian kinetic electron density (G(r)) and the potential electron density (V(r)); the density of the total energy of electrons (H(r))—Cremer-Kraka electronic energy density; the interatomic bond energy, E_{bond}; Figure S12: the 3D structure of HSA divided into six subdomains, each represented in a different color: IA, IB, IIA, IIB, IIIA, and IIIB. Trp214 is highlighted as dark red spheres. The red circle and yellow ellipse indicate the FA8 binding site, located at the edge of the IIA subdomain adjacent to the IIIA subdomain. The FA9 binding site is positioned above, at the level of the IB subdomain, while the FA7 binding site is located deeper within the IIA subdomain, to the left of the FA8 binding site; Table S8: the experimental distances (d) of the coordination bonds between Dy^{3+} ions and nitrate anions or chelate rings in the crystal structure of the **Dy-HMBS-1** complex; Table S9: the experimental distances (d) of the coordination bonds between Dy^{3+} ions and nitrate anions or chelate rings in the crystal structure of the **Dy-HMBS-2** complex; Table S10: the theoretical distances (d) of the coordination bonds between Er^{3+} ions and nitrate anions or chelate rings in the optimized structure of the **Er-HMBS** complex; Table S11: the experimental distances (d) of the coordination bonds between Ni^{2+} ions and nitrate anions or chelate rings in the crystal structure of the **Ni-HMBS** complex; Table S12: the theoretical distances (d) of the coordination bonds between Er^{3+} ions and nitrate anions or chelate rings in the optimized structure of the **V-HMBS** complex.

Author Contributions: Conceptualization, V.J., J.M.Ž., A.A.R. and D.D.; methodology, A.A.A., M.A.A., E.A.A. and O.A.O.A.; software, J.M.Ž., A.A.R. and M.A.H.; validation, A.A.A., M.A.A., O.A.O.A. and M.A.H.; formal analysis, J.M.Ž., A.A.R. and M.A.H.; investigation, A.A.A., M.A.A., E.A.A. and O.A.O.A.; resources, V.J. and M.A.H.; data curation, A.A.A., E.A.A. and M.A.A.; writing—original draft preparation, J.M.Ž. and A.A.R.; writing—review and editing, D.D. and V.J.; visualization, J.M.Ž., M.A.H. and A.A.R.; supervision, D.D.; project administration, V.J. and D.D.; funding acquisition, V.J. All authors have read and agreed to the published version of the manuscript.

Funding: This research was funded by the Scientific Research Deanship at the University of Ha'il, Kingdom of Saudi Arabia, grant number RG-24009.

Institutional Review Board Statement: Not applicable.

Informed Consent Statement: Not applicable.

Data Availability Statement: The data are contained in this article. Further inquiries can be directed to the corresponding author.

Acknowledgments: The authors are thankful to the University of Ha'il, Kingdom of Saudi Arabia. This research was funded by the Scientific Research Deanship at the University of Ha'il, Saudi Arabia, through project number RG-24009.

Conflicts of Interest: The authors declare no conflicts of interest. The funders had no role in the design of the study; in the collection, analyses, or interpretation of data; in the writing of the manuscript; or in the decision to publish the results.

References

1. Casas, J.S.; García-Tasende, M.S.; Sordo, J. Main group metal complexes of semicarbazones and thiosemicarbazones. A structural review. *Coord. Chem. Rev.* **2000**, *209*, 197–261. [CrossRef]
2. Mustafa, Y.F. Modern Developments in the Application and Function of Metal/Metal Oxide Nanocomposite–Based Antibacterial Agents. *Bionanoscience* **2023**, *13*, 840–852. [CrossRef]
3. Pal, R.; Kumar, V.; Gupta, A.K.; Beniwal, V. Synthesis, characterization and DNA photocleavage study of a novel dehydroacetic acid based hydrazone Schiff's base and its metal complexes. *Med. Chem. Res.* **2014**, *23*, 3327–3335. [CrossRef]
4. Padhyé, S.; Kauffman, G.B. Transition metal complexes of semicarbazones and thiosemicarbazones. *Coord. Chem. Rev.* **1985**, *63*, 127–160. [CrossRef]
5. Alsoliemy, A.; Alrefaei, A.F.; Almehmadi, S.J.; Almehmadi, S.J.; Hossan, A.; Khalifa, M.E.; El-Metwaly, N.M. Synthesis, characterization and self-assembly of new cholesteryl-substitued sym-tetrazine: Fluorescence, gelation and mesogenic properties. *J. Mol. Liq.* **2021**, *342*, 117543. [CrossRef]

6. Fernández, M.; Becco, L.; Correia, I.; Benítez, J.; Piro, O.E.; Echeverria, G.A.; Medeiros, A.; Comini, M.; Lavaggi, M.L.; González, M.; et al. Oxidovanadium(IV) and dioxidovanadium(V) complexes of tridentate salicylaldehyde semicarbazones: Searching for prospective antitrypanosomal agents. *J. Inorg. Biochem.* **2013**, *127*, 150–160. [CrossRef] [PubMed]
7. Beraldo, H.; Gambino, D. The Wide Pharmacological Versatility of Semicarbazones, Thiosemicarbazones and Their Metal Complexes. *Mini-Reviews Med. Chem.* **2004**, *4*, 31–39. [CrossRef]
8. Gerasimenko, A.V.; Davidovich, R.L.; Bulimestru, I.G.; Gulea, A.P.; Ng, S.W. Bis(μ-salicylaldehyde semicarbazonato)bis[formatocopper(II)]. *Acta Crystallogr. Sect. E Struct. Rep. Online* **2005**, *61*, m1816–m1817. [CrossRef]
9. Chumakov, Y.M.; Tsapkov, V.I.; Biyushkin, V.N.; Mazus, M.D.; Samus', N.M. Crystal structure of salicylidenesemicarbazidodimethylformamidoaqua- copper(II) salicylidenesemicarbazidodiaquacopper(II) sulfate trihydrate. *Crystallogr. Rep.* **1996**, *41*, 831–836. [CrossRef]
10. Patole, J.; Dutta, S.; Padhye, S.; Sinn, E. Tuning up superoxide dismutase activity of copper complex of salicylaldehyde semicarbazone by heterocyclic bases pyridine and N-methyl imidazole. *Inorganica Chim. Acta* **2001**, *318*, 207–211. [CrossRef]
11. Lee, W.Y.; Lee, P.P.F.; Yan, Y.K.; Lau, M. Cytotoxic copper(ii) salicylaldehyde semicarbazone complexes: Mode of action and proteomic analysis. *Metallomics* **2010**, *2*, 694. [CrossRef] [PubMed]
12. Wang, J.-L.; Liu, B.; Yang, B.-S.; Huang, S.-P. Novel copper(II) complex with unusual π-stacking structure, $[Cu(SSC)Cl]_2 \cdot CH_3OH \cdot 2H_2O$ (SSC = salicylaldehyde semicarbazone anion). *J. Struct. Chem.* **2008**, *49*, 570–574. [CrossRef]
13. Zhang, Y.-F.; Zhou, K.-L.; Lou, Y.-Y.; Pan, D.; Shi, J.-H. Investigation of the binding interaction between estazolam and bovine serum albumin: Multi-spectroscopic methods and molecular docking technique. *J. Biomol. Struct. Dyn.* **2017**, *35*, 3605–3614. [CrossRef]
14. Noblía, P.; Baran, E.J.; Otero, L.; Draper, P.; Cerecetto, H.; González, M.; Piro, O.E.; Castellano, E.E.; Inohara, T.; Adachi, Y.; et al. New Vanadium(V) Complexes with Salicylaldehyde Semicarbazone Derivatives: Synthesis, Characterization, and in vitro Insulin-Mimetic Activity − Crystal Structure of [$V^{V}O_2$ (salicylaldehyde semicarbazone)]. *Eur. J. Inorg. Chem.* **2004**, *2004*, 322–328. [CrossRef]
15. Bogdanovic, G.; Leovac, V.; Vojinovic-Jesic, L.; De, B.-S. Crystal structure of tris(pyridine)(salicylaldehyde semicarbazonato(2-))cobalt(III)-trichloropyridinecobaltate(II) at 293 and 120K. *J. Serbian Chem. Soc.* **2007**, *72*, 63–71. [CrossRef]
16. Mir, I.A.; Ain, Q.U.; Qadir, T.; Malik, A.Q.; Jan, S.; Shahverdi, S.; Nabi, S.A. A review of semicarbazone-derived metal complexes for application in biomedicine and related fields. *J. Mol. Struct.* **2024**, *1295*, 136216. [CrossRef]
17. Binil, P.S.; Anoop, M.R.; Suma, S.; Sudarsanakumar, M.R. Growth, spectral, and thermal characterization of 2-hydroxy-3-methoxybenzaldehyde semicarbazone. *J. Therm. Anal. Calorim.* **2013**, *112*, 913–919. [CrossRef]
18. Vomisescu, C.; Bourosh, P.; Kravtsov, V.; Dragancea, D. Nickel(III) Complex Derived from 2-Hydroxy-3-Methoxybenzaldehyde Semicarbazone and 2,2'-Bipyridine. *Chem. J. Mold.* **2013**, *8*, 78–82. [CrossRef]
19. Chellan, P.; Chibale, K.; Smith, G.S. Molecular Structure of an Unexpected Binuclear Salicylaldimine Semicarbazone Palladium(II) Complex. *J. Chem. Crystallogr.* **2011**, *41*, 747–750. [CrossRef]
20. Bag, P.; Rastogi, C.K.; Biswas, S.; Sivakumar, S.; Mereacre, V.; Chandrasekhar, V. Homodinuclear lanthanide {Ln 2 } (Ln = Gd, Tb, Dy, Eu) complexes prepared from an o-vanillin based ligand: Luminescence and single-molecule magnetism behavior. *Dalt. Trans.* **2015**, *44*, 4328–4340. [CrossRef]
21. Biswas, S.; Das, S.; Hossain, S.; Bar, A.K.; Sutter, J.; Chandrasekhar, V. Tetranuclear Lanthanide(III) Complexes Containing a Square-Grid Core: Synthesis, Structure, and Magnetism. *Eur. J. Inorg. Chem.* **2016**, *2016*, 4683–4692. [CrossRef]
22. Biswas, S.; Das, S.; Rogez, G.; Chandrasekhar, V. Hydrazone-Ligand-Based Homodinuclear Lanthanide Complexes: Synthesis, Structure, and Magnetism. *Eur. J. Inorg. Chem.* **2016**, *2016*, 3322–3329. [CrossRef]
23. Hutchings, A.-J.; Habib, F.; Holmberg, R.J.; Korobkov, I.; Murugesu, M. Structural Rearrangement Through Lanthanide Contraction in Dinuclear Complexes. *Inorg. Chem.* **2014**, *53*, 2102–2112. [CrossRef]
24. Li, M.; Wu, H.; Zhang, S.; Sun, L.; Ke, H.; Wei, Q.; Xie, G.; Chen, S.; Gao, S. Fine-Tuning Ligand Fields with Schiff-Base Ligands in Dy 2 Compounds. *Eur. J. Inorg. Chem.* **2017**, *2017*, 811–819. [CrossRef]
25. Taylor, R.; Wood, P.A. A Million Crystal Structures: The Whole Is Greater than the Sum of Its Parts. *Chem. Rev.* **2019**, *119*, 9427–9477. [CrossRef]
26. Milovanović, M.R.; Stanković, I.M.; Živković, J.M.; Ninković, D.B.; Hall, M.B.; Zarić, S.D. Water: New aspect of hydrogen bonding in the solid state. *IUCrJ* **2022**, *9*, 639–647. [CrossRef]
27. Ninković, D.B.; Janjić, G.V.; Zarić, S.D. Crystallographic and ab Initio Study of Pyridine Stacking Interactions. Local Nature of Hydrogen Bond Effect in Stacking Interactions. *Cryst. Growth Des.* **2012**, *12*, 1060–1063. [CrossRef]
28. Milovanović, M.R.; Živković, J.M.; Ninković, D.B.; Stanković, I.M.; Zarić, S.D. How flexible is the water molecule structure? Analysis of crystal structures and the potential energy surface. *Phys. Chem. Chem. Phys.* **2020**, *22*, 4138–4143. [CrossRef]
29. Spackman, M.A.; Jayatilaka, D. Hirshfeld surface analysis. *CrystEngComm* **2009**, *11*, 19–32. [CrossRef]

30. Kargar, H.; Ardakani, A.A.; Tahir, M.N.; Ashfaq, M.; Munawar, K.S. Synthesis, spectral characterization, crystal structure and antibacterial activity of nickel(II), copper(II) and zinc(II) complexes containing ONNO donor Schiff base ligands. *J. Mol. Struct.* **2021**, *1233*, 130112. [CrossRef]
31. Sinicropi, M.S.; Ceramella, J.; Iacopetta, D.; Catalano, A.; Mariconda, A.; Rosano, C.; Saturnino, C.; El-Kashef, H.; Longo, P. Metal Complexes with Schiff Bases: Data Collection and Recent Studies on Biological Activities. *Int. J. Mol. Sci.* **2022**, *23*, 14840. [CrossRef] [PubMed]
32. Alfonso-Herrera, L.A.; Hernández-Romero, D.; Cruz-Navarro, J.A.; Ramos-Ligonio, Á.; López-Monteon, A.; Rivera-Villanueva, J.M.; Morales-Morales, D.; Colorado-Peralta, R. Transition metal complexes with tetradentate Schiff bases (N_2O_2) obtained from salicylaldehyde: A review of their possible anticancer properties. *Coord. Chem. Rev.* **2024**, *505*, 215698. [CrossRef]
33. Matsia, S.; Papadopoulos, A.; Hatzidimitriou, A.; Schumacher, L.; Koldemir, A.; Pöttgen, R.; Panagiotopoulou, A.; Chasapis, C.T.; Salifoglou, A. Hybrid Lanthanide Metal–Organic Compounds with Flavonoids: Magneto-Optical Properties and Biological Activity Profiles. *Int. J. Mol. Sci.* **2025**, *26*, 1198. [CrossRef] [PubMed]
34. Jevtovic, V.; Rakić, A.; Alshammari, O.A.O.; Alhar, M.S.; Alenezi, T.; Rakic, V.; Dimić, D. Theoretical Study of the Effects of Different Coordination Atoms (O/S/N) on Crystal Structure, Stability, and Protein/DNA Binding of Ni(II) Complexes with Pyridoxal-Semi, Thiosemi, and Isothiosemicarbazone Ligand Systems. *Inorganics* **2024**, *12*, 251. [CrossRef]
35. Harraf, E.; Bikas, R.; Soltani, B.; Lis, T. Synthesis, spectroscopic properties, crystal structure and Hirshfeld surface analysis of Pr(III), Sm(III), Gd(III), Dy(III), and Ho(III) coordination compounds with Schiff base ligand derived from 4-aminoantipyrine. *J. Mol. Struct.* **2024**, *1316*, 139013. [CrossRef]
36. Macedi, E.; Rossi, P.; Formica, M.; Giorgi, L.; Lippi, M.; Montis, R.; Paderni, D.; Paoli, P.; Fusi, V. Crystal structure, Hirshfeld surface analysis and energy framework calculations of different metal complexes of a biphenol-based ligand: Role of solvent and transition metal ion. *J. Mol. Struct.* **2024**, *1299*, 137146. [CrossRef]
37. Hueso-Ureña, F.; Jiménez-Pulido, S.B.; Fernández-Liencres, M.P.; Fernández-Gómez, M.; Moreno-Carretero, M.N. A new five-coordinated CuIP2NO2 system: XRD structure of 6-acetyl-1,3,7-trimethyl-pteridine-2,4(1H,3H)-dione and its Cu(i) (N5,O61,O4)-tridentate complex with triphenylphosphine. An AIM study of the nature of metal–ligand bonds. *Dalt. Trans.* **2008**, *45*, 6461. [CrossRef]
38. Fabijanić, I.; Matković-Čalogović, D.; Pilepić, V.; Ivanišević, I.; Mohaček-Grošev, V.; Sanković, K. New investigations of the guanine trichloro cuprate(II) complex crystal. *J. Mol. Struct.* **2017**, *1128*, 317–324. [CrossRef]
39. Soliman, S.M.; Albering, J.; Abu-Youssef, M.A.M. Structural analyses of two new highly distorted octahedral copper(II) complexes with quinoline-type ligands; Hirshfeld, AIM and NBO studies. *Polyhedron* **2017**, *127*, 36–50. [CrossRef]
40. Lepetit, C.; Vabre, B.; Canac, Y.; Alikhani, M.E.; Zargarian, D. Pentacoordinated, square pyramidal cationic PCP Ni(II) pincer complexes: ELF and QTAIM topological analyses of nickel–triflate interactions. *Theor. Chem. Acc.* **2018**, *137*, 141. [CrossRef]
41. Kasalović, M.P.; Jelača, S.; Milanović, Ž.; Maksimović-Ivanić, D.; Mijatović, S.; Lađarević, J.; Božić, B.; Marković, Z.; Dunđerović, D.; Rüffer, T.; et al. Novel triphenyltin(IV) compounds with carboxylato *N*-functionalized 2-quinolones as promising potential anticancer drug candidates: *In vitro* and *in vivo* evaluation. *Dalt. Trans.* **2024**, *53*, 8298–8314. [CrossRef]
42. Boulechfar, C.; Ferkous, H.; Boufas, S.; Berredjem, M.; Delimi, A.; Djellali, S.; Djedouani, A.; Bahadi, R.; Laamari, S.; Yadav, K.K.; et al. Synthesis, electrochemical, and quantum chemical studies of some metal complexes: Mn(II), Co(II), and Zn(II) with 2-furaldehyde semicarbazone. *J. Mol. Struct.* **2023**, *1271*, 134007. [CrossRef]
43. Jevtovic, V.; Golubović, L.; Alshammari, O.A.O.; Alhar, M.S.; Alanazi, T.Y.A.; Radulović, A.; Nakarada, Đ.; Dimitrić Marković, J.; Rakić, A.; Dimić, D. Structural, Antioxidant, and Protein/DNA-Binding Properties of Sulfate-Coordinated Ni(II) Complex with Pyridoxal-Semicarbazone (PLSC) Ligand. *Inorganics* **2024**, *12*, 280. [CrossRef]
44. Jevtovic, V.; Golubović, L.; Alshammari, B.; Alshammari, M.R.; Rajeh, S.Y.; Alreshidi, M.A.; Alshammari, O.A.O.; Rakić, A.; Dimić, D. Crystal Structure, Theoretical Analysis, and Protein/DNA Binding Activity of Iron(III) Complex Containing Differently Protonated Pyridoxal–S-Methyl-Isothiosemicarbazone Ligands. *Int. J. Mol. Sci.* **2024**, *25*, 7058. [CrossRef] [PubMed]
45. Jevtovic, V.; Golubović, L.; Alshammari, O.A.O.; Alhar, M.S.; Alanazi, T.Y.A.; Rakic, V.; Ganguly, R.; Dimitrić Marković, J.; Rakić, A.; Dimić, D. The Counterion (SO_4^{2-} and NO^{3-}) Effect on Crystallographic, Quantum-Chemical, Protein-, and DNA-Binding Properties of Two Novel Copper(II)–Pyridoxal-Aminoguanidine Complexes. *Crystals* **2024**, *14*, 814. [CrossRef]
46. Papadopoulos, Z.; Doulopoulou, E.; Zianna, A.; Hatzidimitriou, A.G.; Psomas, G. Copper(II) Complexes of 5–Fluoro–Salicylaldehyde: Synthesis, Characterization, Antioxidant Properties, Interaction with DNA and Serum Albumins. *Molecules* **2022**, *27*, 8929. [CrossRef]
47. Shannon, R.D. Revised effective ionic radii and systematic studies of interatomic distances in halides and chalcogenides. *Acta Crystallogr. Sect. A* **1976**, *32*, 751–767. [CrossRef]
48. Allen, F.H. The Cambridge Structural Database: A quarter of a million crystal structures and rising. *Acta Crystallogr. Sect. B Struct. Sci.* **2002**, *58*, 380–388. [CrossRef]

49. Allen, F.H.; Davies, J.E.; Galloy, J.J.; Johnson, O.; Kennard, O.; Macrae, C.F.; Mitchell, E.M.; Mitchell, G.F.; Smith, J.M.; Watson, D.G. The development of versions 3 and 4 of the Cambridge Structural Database System. *J. Chem. Inf. Comput. Sci.* **1991**, *31*, 187–204. [CrossRef]
50. Macrae, C.F.; Bruno, I.J.; Chisholm, J.A.; Edgington, P.R.; McCabe, P.; Pidcock, E.; Rodriguez-Monge, L.; Taylor, R.; van de Streek, J.; Wood, P.A. Mercury CSD 2.0—New features for the visualization and investigation of crystal structures. *J. Appl. Crystallogr.* **2008**, *41*, 466–470. [CrossRef]
51. Turner, M.J.; McKinnon, J.J.; Wolff, S.K.; Grimwood, D.J.; Spackman, P.R.; Jayatilaka, D.; Spackman, M.A. *CrystalExplorer17*; University of Western Australia: Perth, Australia, 2017.
52. Grabowsky, S.; Dean, P.M.; Skelton, B.W.; Sobolev, A.N.; Spackman, M.A.; White, A.H. Crystal packing in the 2-R,4-oxo-[1,3-a/b]-naphthodioxanes—Hirshfeld surface analysis and melting point correlation. *CrystEngComm* **2012**, *14*, 1083–1093. [CrossRef]
53. Frisch, M.J.; Trucks, G.W.; Schlegel, H.B.; Scuseria, G.E.; Robb, M.A.; Cheeseman, J.R.; Scalmani, G.; Barone, V.; Mennucci, B.; Petersson, G.A.; et al. *Gaussian 09, Revision C.01*; Gaussian, Inc.: Wallingford, CT, USA, 2009.
54. Dunning, T.H. Gaussian basis sets for use in correlated molecular calculations. I. The atoms boron through neon and hydrogen. *J. Chem. Phys.* **1989**, *90*, 1007. [CrossRef]
55. Weigend, F.; Ahlrichs, R. Balanced basis sets of split valence, triple zeta valence and quadruple zeta valence quality for H to Rn: Design and assessment of accuracy. *Phys. Chem. Chem. Phys.* **2005**, *7*, 3297. [CrossRef] [PubMed]
56. Weigend, F. Accurate Coulomb-fitting basis sets for H to Rn. *Phys. Chem. Chem. Phys.* **2006**, *8*, 1057. [CrossRef]
57. Dolg, M.; Stoll, H.; Savin, A.; Preuss, H. Energy-adjusted pseudopotentials for the rare earth elements. *Theor. Chim. Acta* **1989**, *75*, 173–194. [CrossRef]
58. Feller, D. The role of databases in support of computational chemistry calculations. *J. Comput. Chem.* **1996**, *17*, 1571–1586. [CrossRef]
59. Schuchardt, K.L.; Didier, B.T.; Elsethagen, T.; Sun, L.; Gurumoorthi, V.; Chase, J.; Li, J.; Windus, T.L. Basis Set Exchange: A Community Database for Computational Sciences. *J. Chem. Inf. Model.* **2007**, *47*, 1045–1052. [CrossRef]
60. Bader, R.F.W. Atoms in molecules. *Acc. Chem. Res.* **1985**, *18*, 9–15. [CrossRef]
61. Bader, R.F.W. A Bond Path: A Universal Indicator of Bonded Interactions. *J. Phys. Chem. A* **1998**, *102*, 7314–7323. [CrossRef]
62. Todd, A. *AIMAll*, version 19.10.12; Keith, T.K., Ed.; Gristmill Software: Overland Park, KS, USA, 2019.
63. Ghuman, J.; Zunszain, P.A.; Petitpas, I.; Bhattacharya, A.A.; Otagiri, M.; Curry, S. Structural Basis of the Drug-binding Specificity of Human Serum Albumin. *J. Mol. Biol.* **2005**, *353*, 38–52. [CrossRef]
64. Morris, G.M.; Huey, R.; Lindstrom, W.; Sanner, M.F.; Belew, R.K.; Goodsell, D.S.; Olson, A.J. AutoDock4 and AutoDockTools4: Automated docking with selective receptor flexibility. *J. Comput. Chem.* **2009**, *30*, 2785–2791. [CrossRef] [PubMed]
65. Valdés-Tresanco, M.S.; Valdés-Tresanco, M.E.; Valiente, P.A.; Moreno, E. AMDock: A versatile graphical tool for assisting molecular docking with Autodock Vina and Autodock4. *Biol. Direct* **2020**, *15*, 12. [CrossRef] [PubMed]

Disclaimer/Publisher's Note: The statements, opinions and data contained in all publications are solely those of the individual author(s) and contributor(s) and not of MDPI and/or the editor(s). MDPI and/or the editor(s) disclaim responsibility for any injury to people or property resulting from any ideas, methods, instructions or products referred to in the content.